

# Secondary electron emission and yield spectra of metals from Monte Carlo simulations and experiments

Martina Azzolini<sup>1,2</sup>, Marco Angelucci<sup>3</sup>, Roberto Cimino<sup>3</sup> ,  
Rosanna Larciprete<sup>3,4</sup>, Nicola M Pugno<sup>2,5,6</sup> , Simone Taioli<sup>1,7</sup>   
and Maurizio Dapor<sup>1</sup>

<sup>1</sup> European Centre for Theoretical Studies in Nuclear Physics and Related Areas (\*ECT\*-FBK) and Trento Institute for Fundamental Physics and Applications (TIFPA-INFN), Trento, Italy

<sup>2</sup> Laboratory of Bio-Inspired and Graphene Nanomechanics—Department of Civil, Environmental and Mechanical Engineering, University of Trento, Trento, Italy

<sup>3</sup> Laboratori Nazionali di Frascati (INFN), Frascati (RM), Italy

<sup>4</sup> Institute for Complex System (CNR), Rome, Italy

<sup>5</sup> School of Engineering and Materials Science, Materials Research Institute, Queen Mary University of London, London, United Kingdom

<sup>6</sup> Ket Lab, Edoardi Amaldi Foundation, c/o Italian Space Agency, Rome, Italy

<sup>7</sup> Faculty of Mathematics and Physics, Charles University, Prague, Czech Republic

E-mail: [mazzolini@ectstar.eu](mailto:mazzolini@ectstar.eu), [taioli@ectstar.eu](mailto:taioli@ectstar.eu) and [dapor@ectstar.eu](mailto:dapor@ectstar.eu)

Received 12 September 2018, revised 16 November 2018

Accepted for publication 23 November 2018

Published 19 December 2018



## Abstract

In this work, we present a computational method, based on the Monte Carlo statistical approach, for calculating electron energy emission and yield spectra of metals, such as copper, silver and gold. The calculation of these observables proceeds via the Mott theory with a Dirac–Hartree–Fock spherical potential to deal with the elastic scattering processes, and by using the Ritchie dielectric approach to model the electron inelastic scattering events. In the latter case, the dielectric function, which represents the starting point for the evaluation of the energy loss, is obtained from experimental reflection electron energy loss spectra. The generation of secondary electrons upon ionization of the samples is also implemented in the calculation. A remarkable agreement is obtained between both theoretical and experimental electron emission spectra and yield curves.

Keywords: secondary electron emission, Monte Carlo method, noble metals, yield

(Some figures may appear in colour only in the online journal)

## 1. Introduction

The emission of secondary electrons plays a fundamental role in materials characterization techniques [1, 2], such as scanning electron microscopy [3, 4], and in affecting the performance of a variety of electron devices, such as the detectors based on electron multipliers [5, 6]. These techniques in particular seek a high value of the electron yield to reach a low noise-to-signal ratio for enhancing the image quality. High electron yield can be achieved by coating the photomultiplier

with low work function photocathode or by increasing the local curvature of the surface by steep edges.

On the other hand, in other applications the emission of secondary electrons must be suppressed, e.g. in particle accelerators. Indeed, detrimental effects on the machine stability, which might result in beam loss [7–12], can be caused by the so-called multipactor effect. This phenomenon appears when the current of re-emitted electrons grows uncontrollably due to presence of electronic charges in proximity of the vacuum tube walls. The latter are accelerated by the primary beam,

producing an avalanche of secondary electrons. In this regard, chemical treatment, coating [13, 14] and patterning of the target surface [15–18] were used to overcome the harmful effects brought about by this phenomenon. Analogous criticality concerns microwave and RF components for space applications that find one of their most important functional limitations in the multipactor and corona breakdown discharges [19].

Despite these remarkable attempts, several issues could be bypassed by developing an efficient and accurate method to calculate the electron yield of the investigated material, in order to predict the secondary emission and thus to tailor the solution according to the application sought for. In this regard, analytic descriptions of the secondary electron energy yield have been developed over the years [20–24].

In this work, we present an accurate computational approach, based on the Monte Carlo method [25], to simulate electron trajectories leading to secondary electron emission and we compare theoretical lineshapes with our recorded experimental yield spectra. Within this approach, elastic collision and inelastic scattering processes are carefully evaluated. In the former case this means to assess the angular deviation along the path of the electrons in their way out of the solid, while in the latter the electron energy loss. In particular, the elastic scattering is treated within the Mott theory [26] using a Dirac–Hartree–Fock spherical potential, while the inelastic scattering events are dealt with the Ritchie dielectric theory [27]. The Monte Carlo method is used to simulate the secondary spectra of three metallic targets, that is copper, silver and gold. The dielectric functions used in the assessment of the energy loss of these materials are obtained from reflection electron energy loss (REEL) experiments [28]. This treatment thus takes into account the contribution to the secondary emission spectra of both bulk and surface plasmon excitations, increasing the accuracy of the computed data.

This paper is structured as follows: in the following section 2 the experimental procedures used in the measurements of the secondary emission and yield spectra of all metals are described. Afterwards, a detailed discussion of the computational Monte Carlo approach is presented in section 3. Finally, in section 4 we present a thorough comparison between simulated and experimental data of secondary emission and yield spectra.

## 2. Experimental details

The experimental apparatus used to study the secondary electron yield (SEY) and angle integrated energy distribution curves (EDC) is hosted in the ‘Material Science’ laboratory of LNF-INFN, Frascati (Rome). For our experiments we used a specially built UHV  $\mu$ -metal chamber with less than 5 mGauss residual magnetic field at the sample position, pumped by a CTI8 cryopump to ensure a vacuum better than  $10^{-10}$  mbar. The set-up has been designed to limit the residual magnetic field near the sample, which can deviate low-energy electrons. Ion pumps are not used due to their detrimental stray magnetic field. This set up is routinely measuring SEY

curves from very low primary energies to about 1000 eV [9–12, 29, 30]. The SEY, i.e. the ratio of the number of electrons leaving the sample surface ( $I_s$ ) to the number of incident electrons ( $I_p$ ) per unit area, was determined experimentally by measuring  $I_p$  and the total sample current  $I_t = I_p - I_s$ , so that  $\delta = 1 - I_t/I_p$ . For the SEY measurements, the electron beam was set to be smaller than  $1 \text{ mm}^2$  in transverse cross-sectional area at the sample surface. To measure the current of the impinging primary electrons, a negative bias voltage ( $-75 \text{ V}$ ) was applied to the sample. The SEY measurements were performed at normal incidence, by using electron beam currents of a few nA. A SpectraLEED Omicron LEED/Auger retarding field (RF) analyser system was specially modified to be able to collect angle integrated EDC with RF filtering and computer control while using the gun in LEED mode, i.e. with a low-energy focused beam. The  $e^-$  gun provided a small and stable (both in current and position) beam spot on the sample, in the energy range from 30 to 1000 eV. This set-up can measure angle integrated EDC with the limitation typical of any RF analyzers. While the secondaries are consistently measured at all primary energies, elastic peaks broaden due to increasingly poor resolution at higher primary energies, showing an additional strong asymmetry on the low energy side due to the integration of the background [31, 32]. Despite those known limitations, the data can be used in this work to extract the relevant information needed. The sample can be transferred from air into UHV conditions and can be cooled down to 10 K, exposed to various types of gases and cleaned by subsequent cycles of Ar sputtering. All the polycrystalline metallic samples here studied were cleaned by repeated  $\text{Ar}^+$  sputtering cycles at 1.5 KeV in Ar pressure of  $5 \times 10^{-6}$  mbar until no signal of C and O was observed in the XPS spectrum.

## 3. Computational details

### 3.1. Monte Carlo

The Monte Carlo approach models the spectral distribution of energy transferred to a specimen bombarded with a perpendicularly incident electron beam by following the electron trajectories within the target. The electron trajectories result from the elastic and inelastic interactions undergone by the electrons scattered by the nuclei and the electron clouds of target atoms, respectively.

Secondary electrons are generated via inelastic interactions through the ionization of the target’s atomic centers. In the latter process, by measuring the kinetic energies of the escaping charges, the electron emission energy spectra can be recorded. In the Monte Carlo simulation of this emission mechanism the trajectories of secondary electrons, similarly to those generated by elastic and non-ionizing inelastic scattering, are followed by using a statistical algorithm. At variance, the path of electrons with kinetic energies below the value of the work function or of electrons emitted by the specimen is considered terminated.

In Monte Carlo simulations, the probability of elastic and inelastic scattering events is assessed by comparing random numbers with the correspondent probability distributions.

These probability distributions are calculated by using the elastic and inelastic cross sections, computed via the Mott [26] and the Ritchie dielectric theories [27], respectively. These models and the relevant distribution probabilities will be presented in detail in the sections 3.2 and 3.3.

The incident electron beam direction is set perpendicular to the specimen surface and the kinetic energy is increased by the specific target work function  $\chi$ . Upon elastic and inelastic scattering events, the electron trajectory can reach the target surface. Finally, electrons can be emitted from the sample provided that the following condition is satisfied:

$$E \cos^2 \theta \geq \chi, \quad (1)$$

where  $\theta$  is the angle between the scattering direction inside the material and the normal to the target surface, and  $E$  is the electron kinetic energy. This condition stems from the fact that the target-vacuum interface represents an energy barrier to be overcome by the escaping electrons at the interface. Finally, the electron emission is determined by assessing the transmission coefficient  $t$ , which can be obtained by assuming that the electrons feel a model step potential at the surface [33]:

$$t = \frac{4\sqrt{1 - \chi/(E \cos^2 \theta)}}{\left[1 + \sqrt{1 - \chi/(E \cos^2 \theta)}\right]^2}. \quad (2)$$

In our Monte Carlo approach the transmission coefficient is compared with a random number  $\mu_2$ , uniformly sampled in the interval [0,1] so that for  $\mu_2 < t$  the electrons is emitted from the surface with a kinetic energy decreased by the work function  $\chi$ , otherwise electrons are elastically reflected back and continue their path within the solid target. Here we notice that  $\chi$  plays a key role in the electron emission process, and we do expect a dramatic dependence of the electron yield from this observable. This effect will be discussed thoroughly in section 4.3.

### 3.2. Elastic scattering

The elastic scattering between electrons and target nuclei is described by the Mott theory [26]. The differential elastic scattering cross section ( $d\sigma_{el}/d\Omega$ ) can be written as:

$$\frac{d\sigma_{el}}{d\Omega} = |f|^2 + |g|^2 \quad (3)$$

where  $f$  and  $g$  are the scattering amplitudes [33, 34], which can be obtained by solving the Dirac equation in a central field. For the materials under investigation in this work, that is Cu, Ag and Au, the calculation of the elastic scattering cross section was performed using the analytic formulation of the atomic potential proposed by Salvat [35]. The total elastic scattering cross section  $\sigma_{el}(E)$  is obtained by integrating equation (3) in the solid angle. The results are shown in figure 1 and compared with the tabulated values of [36]. We notice that the elastic cross sections obtained by using the Mott theory with a Dirac–Hartree–Fock (DHF) potential and those from the NIST database differ significantly at low energies for all investigated cases, that is below 100 eV. This is due to the treatment of the exchange potential, and of the correlation-polarization

and absorption corrections in the calculation of the differential elastic cross-section, which in ELSEPA are lumped together in an effective optical-model potential (‘static-field approximation’) [37]. While for energies higher than about 1 keV, the (relative) magnitudes of the polarization and absorption corrections decrease when  $E$  increases, they become appreciable for relatively slow projectiles. Thus, the reliability of a semi-empirical optical-model potential below 50 eV might be questioned due to the increasing importance of the correlation effects [37]. Nevertheless, being our goal the simulation of the secondary electron emission typically characterized by low energies, one needs to follow the electron path up to kinetic energies as low as 1 eV. Thus, unfortunately ELSEPA cross sections are unsafe in the needed energy range and we must rely on the Mott’s model using the Dirac–Hartree–Fock potential (Mott+DHF). We notice that in this case we do not include solid-state effects. Thus we do not use potentials that take into account the presence of a charge distribution different from free atoms, which usually results in smaller differential cross sections in the former case than in the latter.

From the knowledge of the function  $\sigma_{el}(E)$ , one can calculate the elastic scattering mean free path ( $\lambda_{el}$ ) at a given kinetic energy as follows:

$$\lambda_{el}(E) = \frac{1}{N\sigma_{el}(E)}, \quad (4)$$

where  $N$  is the atomic density. In our MC model, the elastic scattering events lead to a change in the direction of the electron path. The scattering angle  $\bar{\theta}$  after an elastic collision can be evaluated by calculating the cumulative elastic scattering probabilities  $P_{el}(\bar{\theta}, E)$  for different values of the electron kinetic energies  $E$  (see figure 2):

$$P_{el}(\bar{\theta}, E) = \frac{2\pi}{\sigma_{el}(E)} \int_0^{\bar{\theta}} \frac{d\sigma_{el}(E)}{d\Omega} \sin \theta d\theta. \quad (5)$$

Finally,  $\bar{\theta}$  can be assessed by equalizing  $P_{el}$  at a given electron kinetic energy with a random number  $\mu_3$ , which is sampled uniformly in the interval [0, 1].

### 3.3. Inelastic scattering and secondary electron generation

Inelastic scattering between the electrons in the beam and in the target atoms slows down the charge motion along the path. The electrons moving within the solid may transfer a fraction of their kinetic energy to the target’s atomic electron cloud, producing both excitations and ionizations. These processes can be fully described by the dielectric theory of Ritchie [27]. The dielectric function  $\epsilon(W, \vec{q})$ , which depends on transferred energy  $W$  and momentum  $\vec{q}$ , describes the ‘tendency’ of a solid to be polarized by an incoming charged particle or electromagnetic wave. The dielectric function can be assessed by both experiments and simulations [38, 39]. Recently, it is possible to acquire emission electron energy loss spectra with acceptable energy resolutions. This allows the calculation of surface and bulk plasmon excitations as reported by Narayan *et al* [40, 41]. In this case, we decided to use the dielectric function obtained from experimental reflection electron

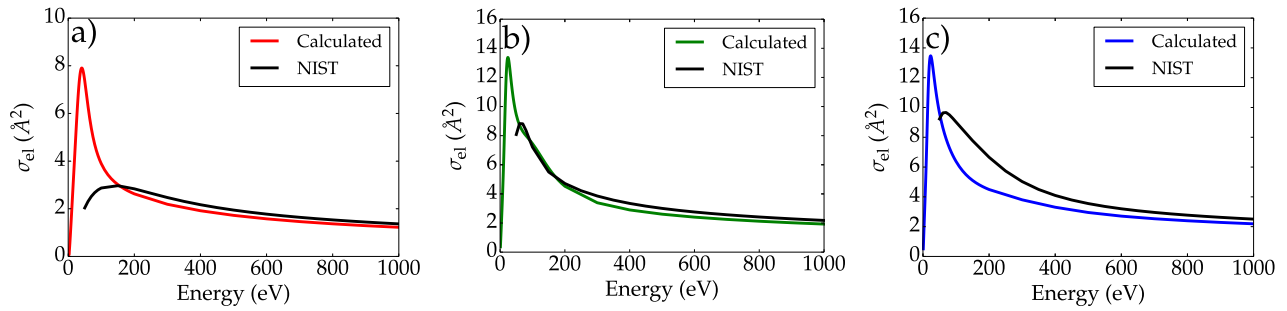


**Figure 1.** Total elastic scattering cross sections of (a) Cu, (b) Ag, and (c) Au as a function of the electron kinetic energy. Black lines report tabulated values from [36].

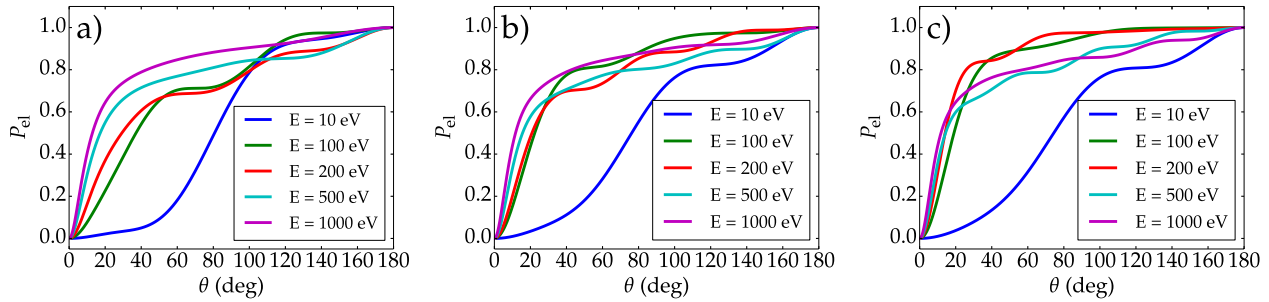


**Figure 2.** Cumulative elastic scattering probabilities of (a) Cu, (b) Ag, and (c) Au as a function of the scattering angle for several kinetic energies.

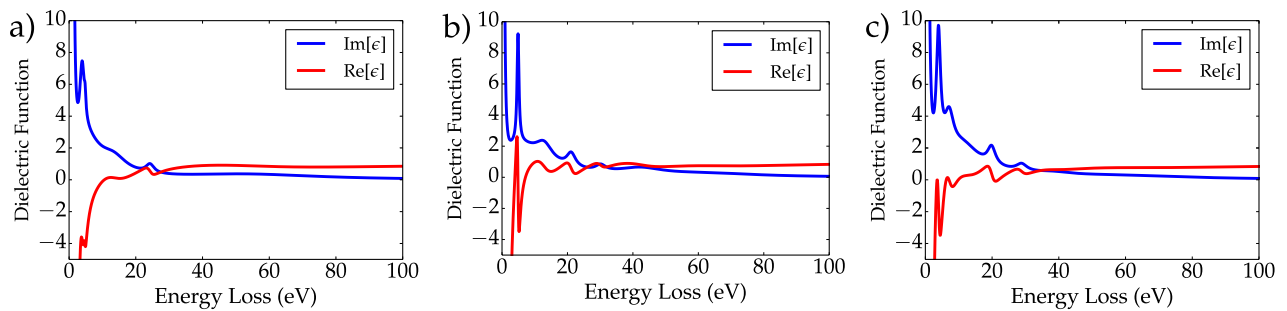


**Figure 3.** Real (red) and imaginary (blue) components of the dielectric functions of (a) Cu, (b) Ag, and (c) Au, as a function of energy loss for vanishing transferred momentum, obtained by using the fitting parameters reported in [28].

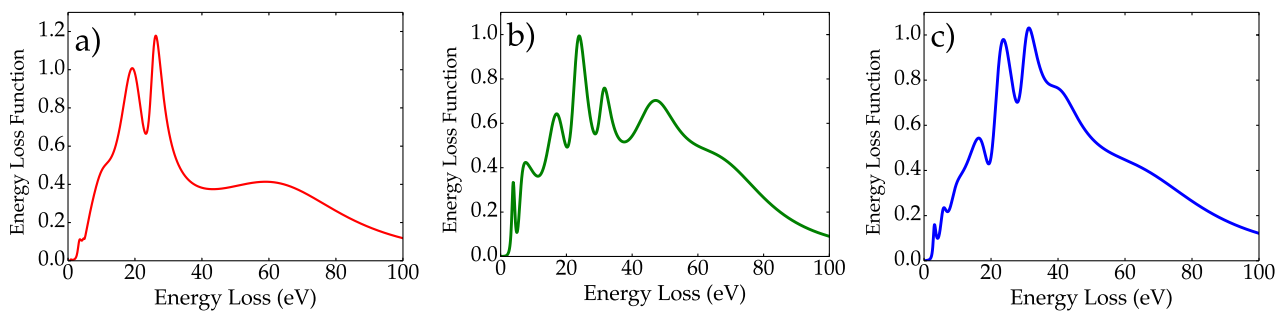


**Figure 4.** Energy loss functions of (a) Cu, (b) Ag, and (c) Au as a function of energy loss and for vanishing transferred momentum obtained using the fitting parameters provided in [28].

energy loss spectra by Werner *et al* [28], as it includes both the bulk and the surface contributions to the electronic excitation. The real and imaginary components of the dielectric function were fitted via Drude–Lorentz functions, which mimic plasmon oscillations, whose fitting parameters are provided in [28]. In figure 3 we show the dependence on the energy loss of

the real and imaginary parts of the dielectric functions of Cu, Ag and Au for vanishing transferred momentum.

From the knowledge of the dielectric function, one can obtain the key quantity in charge transport Monte Carlo simulations, that is the energy loss function (ELF) defined by the following relation:

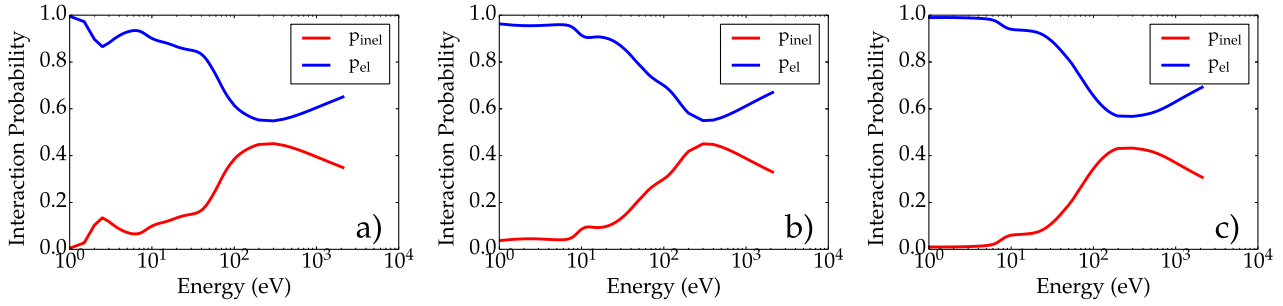


**Figure 5.** Elastic (blue line) and inelastic (red line) scattering probabilities of (a) Cu (a), (b) Ag, and (c) Au as a function of the electron energy.

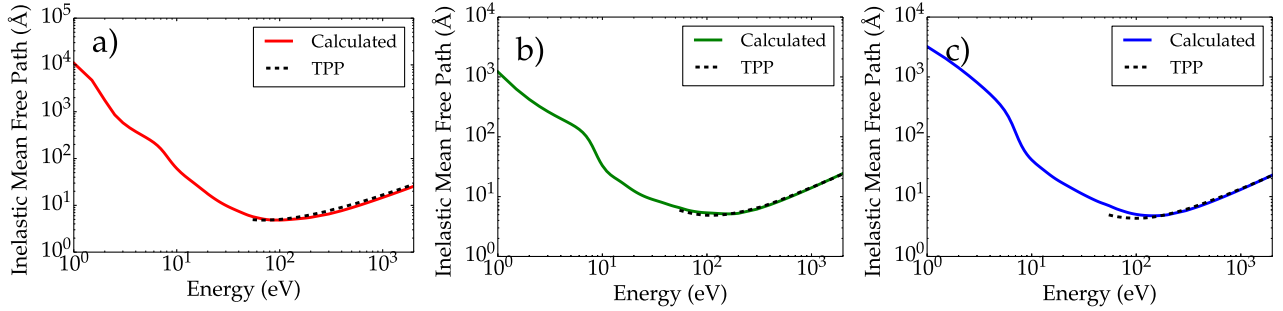


**Figure 6.** Inelastic mean free paths of (a) Cu, (b) Ag, and (c) Au as a function of the electron kinetic energy. Dashed lines show the data obtained by Tanuma *et al* [42].

$$\text{ELF} = \text{Im} \left[ -\frac{1}{\epsilon(q, W)} \right] = \frac{\text{Im}[\epsilon]}{\text{Re}[\epsilon]^2 + \text{Im}[\epsilon]^2}. \quad (6)$$

Using the formula (6), the ELF of Cu, Ag, and Au were calculated and are shown in figure 4. While our electron loss functions are ultimately derived from reflection EELS measurements, so that multiple scattering and surface losses overlap with the bulk electron loss function, we notice that recent transmission electron loss measurements [40, 41] may have enough resolution and accuracy to separate the different components.

To extend the dielectric function to transferred momenta  $\vec{q}$  different from zero we apply the following dispersion law to the characteristic energies of the oscillators  $W_i(q)$ :

$$W_i(q) = W_i(q=0) + \alpha \frac{(\hbar q^2)}{2m} \quad (7)$$

where  $m$  is the electron mass,  $q$  the modulus of the transferred momentum, and  $\alpha$  a dispersion coefficient that depends on the energy scale. Indeed, the Drude–Lorentz theory was developed to describe excitations in the low energy region, corresponding to energy losses lower than the semi-core transition energies. To extend properly the Drude–Lorentz theory to higher energies the  $\alpha$  dispersion parameter must be tuned. According to [28], we set  $\alpha = 1$  for oscillator energies  $W_i(q=0)$  lower than the characteristic energies of the semi-core transitions. For larger oscillators energy,  $\alpha$  was set to 0.5, a value which ensures the best agreement with experimental measurements [28]. The threshold energies of the semi-core transitions are  $E_{3p_{3/2}} = 75.1$  eV for Cu,  $E_{5p_{3/2}} = 57.2$  eV for Ag, and  $E_{4p_{3/2}} = 58.3$  eV for Au respectively [28].

The knowledge of the ELF can be used for calculating the differential inverse inelastic mean free path (DIIMFP), which is defined as:

$$\frac{d\lambda_{\text{inel}}^{-1}}{dW} = \frac{1}{\pi a_0 E} \int_{q_-}^{q_+} \frac{dq}{q} \text{Im} \left[ -\frac{1}{\epsilon(q, W)} \right] \quad (8)$$

where  $a_0$  is the Bohr radius and the integration limits are  $q_{\pm} = \sqrt{2mE} \pm \sqrt{2m(E-W)}$ , with  $W$  the transferred energy. The total inelastic mean free path  $\lambda_{\text{inel}}$  (IMFP) is obtained by integrating the DIIMFP in the energy loss range  $[0, E/2]$ , where  $E/2$  is the largest value that an electron undergoing inelastic collisions can lose. In figures 6(a)–(c) we present the IMFPs of Cu, Ag, and Au respectively compared with the simulations performed by Tanuma *et al* [42].

The tendency of electrons to undergo elastic or inelastic collisions can be assessed by their respective distribution probabilities,  $p_{\text{el}} = \lambda_{\text{tot}}/\lambda_{\text{el}}$  and  $p_{\text{inel}} = \lambda_{\text{tot}}/\lambda_{\text{inel}}$ , while the total mean free path  $\lambda_{\text{tot}}$  is defined by the following relation:

$$\lambda_{\text{tot}}^{-1}(E) = \lambda_{\text{inel}}^{-1}(E) + \lambda_{\text{el}}^{-1}(E). \quad (9)$$

The MC scheme applied to the electron transport within solids proceeds in the following way: a random number  $\mu_4$  uniformly distributed in the range  $[0, 1]$  is generated and compared with  $p_{\text{inel}}$ . Should the condition  $\mu_4 < p_{\text{inel}}$  be satisfied, the collision is classified as inelastic, otherwise is elastic. In figure 5 we plot the elastic (blue line) and inelastic (red line) probabilities for different values of the electron kinetic energy.

As a results of the inelastic scattering event, the impinging electron loses a fraction  $\bar{W}$  of its kinetic energy. In the MC calculation, the value of  $\bar{W}$  is determined for each inelastic collision by comparing a random number  $\mu_5$  (uniformly distributed in the interval  $[0, 1]$ ), with the correspondent

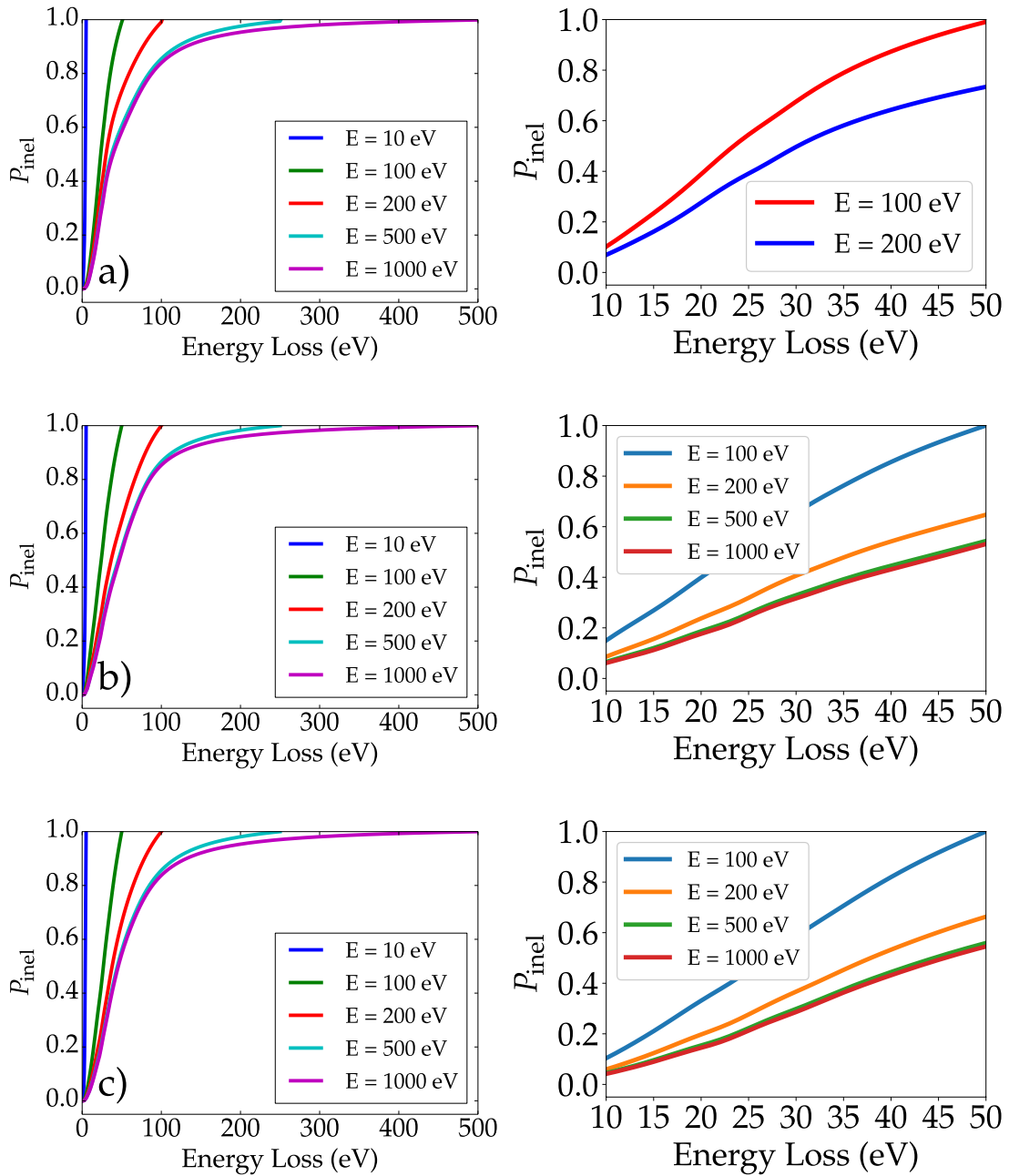


**Figure 7.** Left panels: cumulative inelastic scattering probabilities of (a) Cu, (b) Ag, and (c) Au as a function of the energy loss for different kinetic energies. Right panels: relevant zoom showing the shoulders due to surface and bulk plasmons.

cumulative probability distribution  $P_{\text{inel}}(E, W)$ . These probabilities are calculated for different values of the electron kinetic energies  $E$  (see figure 7), as:

$$P_{\text{inel}}(E, \bar{W}) = \lambda_{\text{inel}}(E) \int_0^{\bar{W}} \frac{d\lambda_{\text{inel}}^{-1}(E, W)}{dW} dW. \quad (10)$$

The value of  $\bar{W}$  for which the value of  $P_{\text{inel}}$  is equal to  $\mu_5$  is the energy loss upon one inelastic collision. Thus, the electron kinetic energy will be decreased by this value. The angular deviation due to inelastic scattering is evaluated according to the classical binary collision theory.

Moreover, should the energy loss be larger than the first ionization energy  $B$  (that is, the energy required to extract one

**Table 1.** Characteristic quantities of the target materials: density (second column) and mean ionization energy  $\langle B \rangle$  (third column).

Metal	Density ( $\text{g cm}^{-3}$ )	$\langle B \rangle$ (eV)
Cu	8.96 [43]	7.726
Ag	10.5 [42]	7.576
Au	19.32 [44]	9.226

electron from the outer electron shell of the target atom), a secondary electron is emitted with kinetic energy equal to  $\bar{W} - B$ . After the ionization event, the generated secondary electron moves inside the solid target as any other particle, due to the indistinguishability of the electrons.

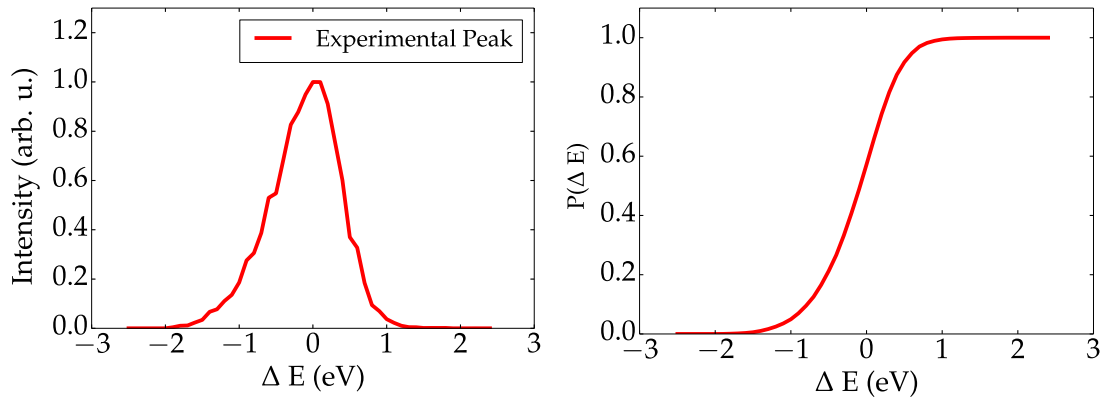


**Figure 8.** (a) Experimental elastic peak of copper; (b) Cumulative probability distribution of the experimental elastic peak.

## 4. Results and discussion

In our MC simulations we considered copper, silver and gold bulk metals as test cases of our method. In table 1 the characteristics of these materials are reported. In the next sections we present both electron emission spectra and yield curves of these three metals.

### 4.1. Determination of initial kinetic energy of the electron beam

The starting point of charge transport Monte Carlo calculations is to determine the initial kinetic energy and the cumulative distribution probability of the primary beam impinging on the surface target. The kinetic energy can be obtained from our experiments by considering the energy distribution of the elastic peak, generated by the electrons which have been elastically reflected by the target surface. These electrons are recorded around a sharp peak at energies  $\bar{E} \pm \Delta E$ , where  $\bar{E}$  is the energy of the peak maximum and  $\Delta E$  takes into account the width of the kinetic energy distribution. In particular, in this work we used the experimental elastic peak distribution of copper  $f(\Delta E)$ , which is reported in figure 8(a). This elastic distribution is conventionally centered in zero. Then, the cumulative distribution probability (see figure 8(b)) is computed as a function of the energy correction by using the following expression:

$$P(\Delta E) = \frac{1}{\text{Area}} \int_{E_-}^{\Delta E} f(\Delta E') d(\Delta E') \quad (11)$$

where the total area of the peak (Area) was calculated by integrating the experimental  $f(\Delta E)$  curve in the symmetric energy interval  $[E_-, E_+]$ , with  $E_{\pm} = \pm 2.5$  eV as follows:

$$\text{Area} = \int_{E_-}^{E_+} f(\Delta E') d(\Delta E'). \quad (12)$$

The value of the correction  $\Delta E$  to the maximum  $\bar{E}$  of the elastic peak has to be determined to set the initial kinetic energy for each electron in the primary beam. This is accomplished by generating a random number  $\mu_1$ , uniformly distributed in the interval  $[0,1]$ , and by finding the value of  $\Delta E$  for which  $P(\Delta E)$  in equation (11) is equal to  $\mu_1$ . Finally, the initial kinetic energy of each electron in the primary beam is set

to  $\bar{E} + \Delta E$  and the Monte Carlo evaluation of its trajectory within the solid resulting from elastic, inelastic and ionizing events can be pursued.

### 4.2. Full energy emission spectra of Cu

MC simulations were performed to calculate the full energy emission spectrum of bulk copper for different energies  $E$  of the primary beam. The number of electrons in the beam was set to  $10^7$  to obtain stable results. The sample work function was set to 5.4 eV.

The initial electron kinetic energy is distributed according to the experimental elastic peak of copper reported in the previous figure 8. Emitted electrons are collected as a function of their kinetic energies. Theoretical spectra are compared with our experimental data for different initial kinetic energies in figure 9. The panels on the left side of this figure report the spectra normalized at a common height of the secondary electron (SE) emission peak, while the right panels show the spectra normalized at a common area.

As it is reported above, we notice that the experimental spectra were acquired with a (RF) analyzer which is known to cause a characteristic broadening of the elastic peak due to poor resolution at high energies and a strong asymmetry on the low energy side due to the integration of the background [31, 32]. Thus, the integrated area of the whole elastic peak is always higher than that obtained by our MC simulations [45, 46]. This is the reason why the MC secondary electron peaks are more intense than the experimental ones when the spectra are normalized at a common area (see the panels at the right side of figure 9). Nevertheless, by normalizing to a common height of the secondary electron emission peak, a remarkable agreement is obtained between the secondary electrons MC and the experimental lineshapes.

### 4.3. Electron yield

The electron yield is defined as the total number of emitted electrons divided by the number of electrons in the beam. This quantity was calculated in the case of Cu, Ag and Au for different initial kinetic energies. To calculate the electron yield spectra, we set to  $10^6$  the number of electrons in the beam. In figure 10 we compare the theoretical electron yield

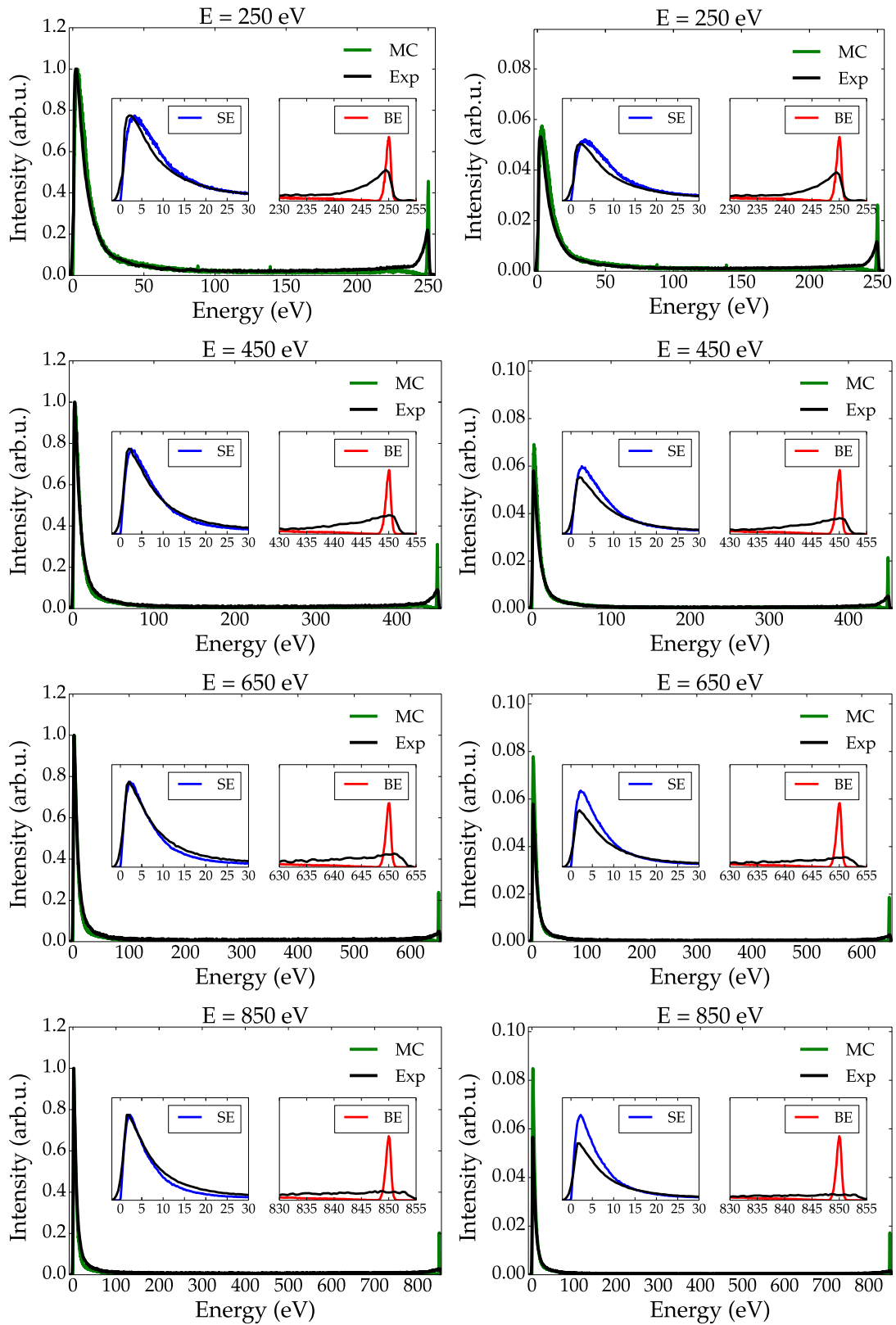


**Figure 9.** Electron energy emission spectra of Cu for different initial kinetic energies. The panels on the left side of the figure report spectra normalized at a common height of the secondary electron emission peak, while the panels on the right show spectra normalized at a common total area of the spectrum. The insets in each panel display the two main contributions to the spectra, that is the secondary electron (SE) emission peak (blue curve) and the back-scattered electrons (BE, red curve), respectively. The experimental data are shown as black lines.

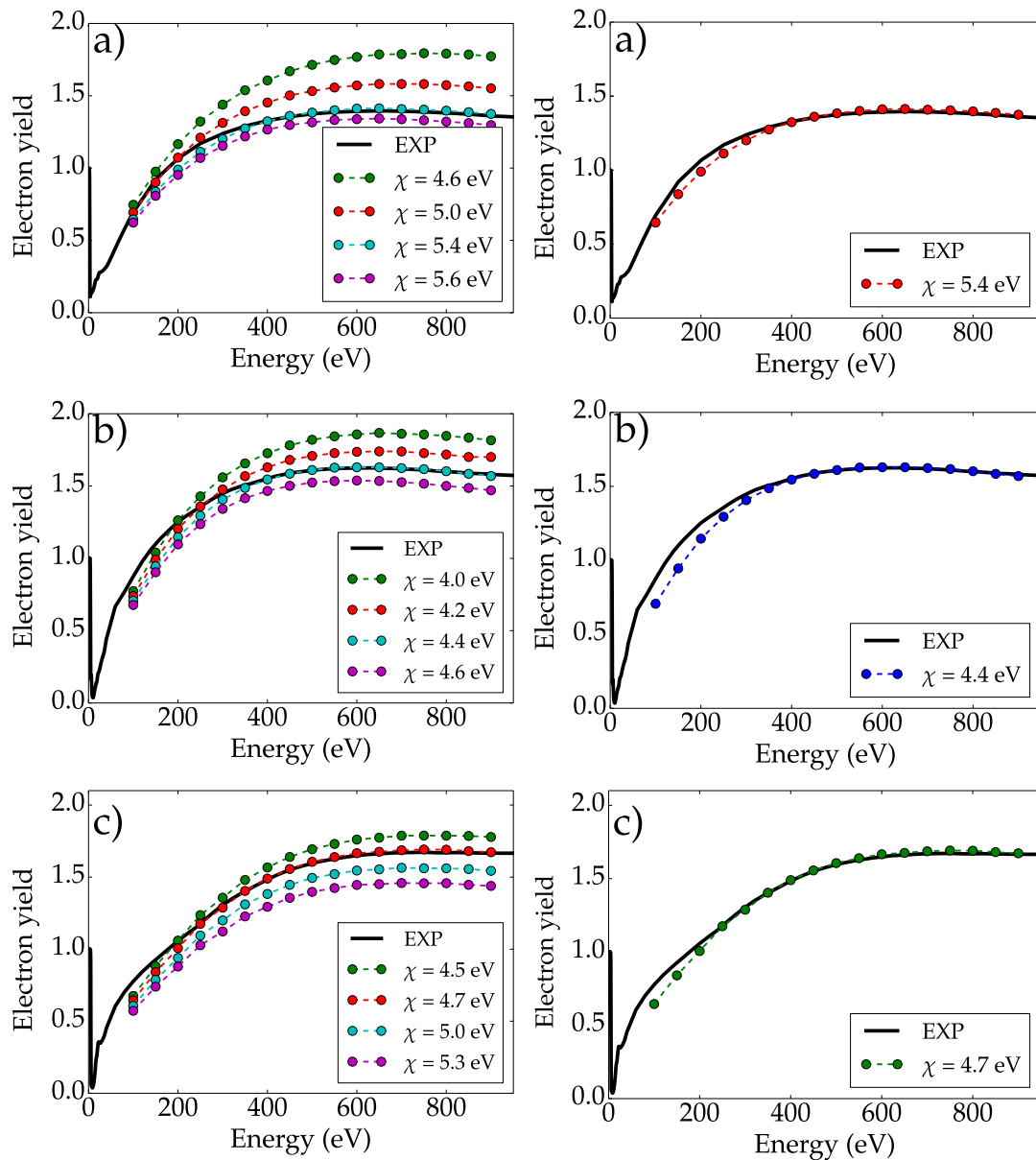


**Figure 10.** Electron yield curves of (a) Cu, (b) Ag, and (c) Au as a function of the initial primary electron beam kinetic energy, for different values of the work functions  $\chi$  (left panels). Black lines report the experimental data [30]. In the right hand side we report the yield spectra for the value of the work function leading to the best agreement between simulations and experiments.

curves with the experimental data by Gonzales *et al* [30], all recorded on polycrystalline atomically sputtered clean noble metals. We notice that the measured work functions fit well with values reported in the literature [47]. In the left hand side of figure 10 we tested the dependence of the yield upon a reasonable change of the work function  $\chi$ : thus, different simulations were carried out by changing this parameter.

These results show that spectra calculated with a higher value of  $\chi$  display lower intensities than those obtained with a lower  $\chi$ . This finding reflects the fact that an increase of the emission energy barrier, that is the work function, results in a decreasing number of electrons emerging from the surface. The best agreement with the experimental data [30] is obtained

for  $\chi = 5.4$  eV for copper (experimental value is 4.6 eV [30]),  $\chi = 4.4$  eV for silver (experimental value is 4.4 eV [30]), and  $\chi = 4.7$  eV for gold (experimental value is 5.3 eV [30]), respectively. We notice that for silver we are able to reproduce the yield experimental spectra with an exceptional agreement of the work function between simulations and measurements. In the case of copper and gold this agreement is anyway rather good. Furthermore, in figure 11 we compare the secondary electron yields of (a) Cu, (b) Ag, and (c) Au calculated from Monte Carlo simulations using the Mott+DHF (filled blue circles) and the NIST (filled orange circles) [36] differential elastic cross sections, respectively.

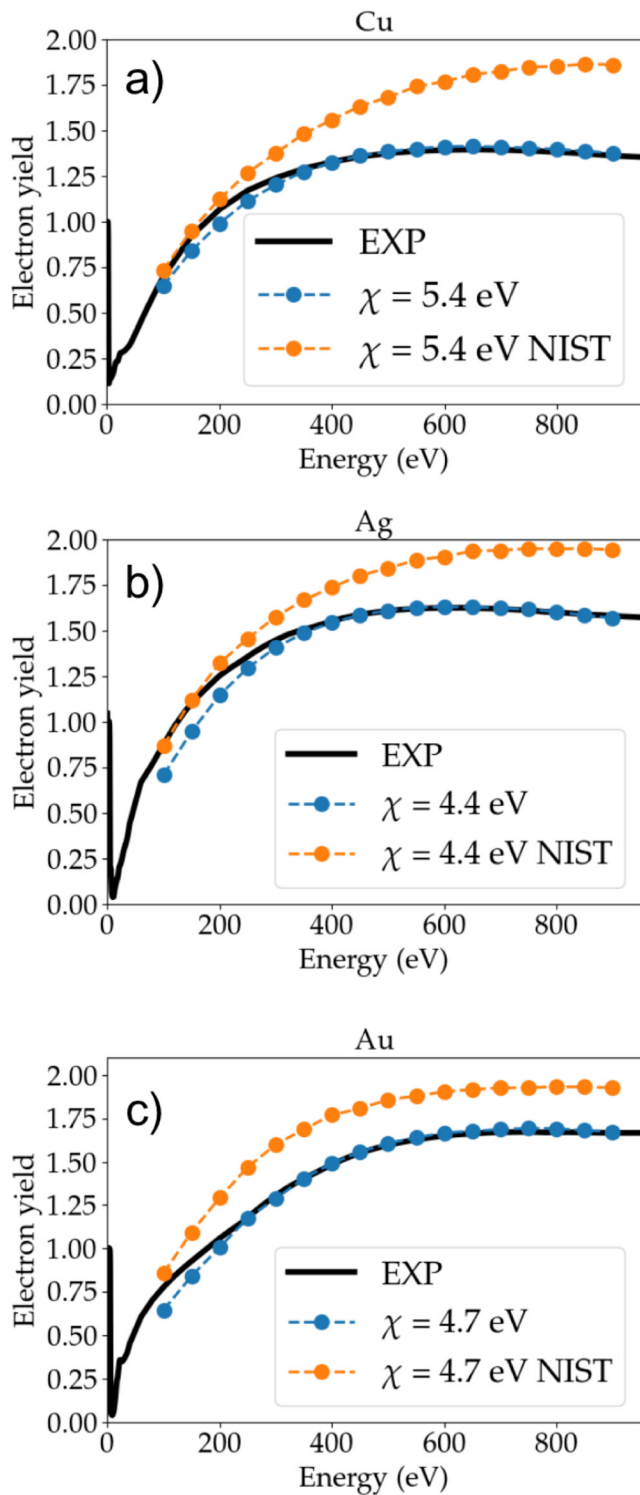


**Figure 11.** SEY for (a) Cu, (b) Ag, and (c) Au calculated by using the Mott + DHF cross section (blue circles), the NIST database (orange circles) [36] in comparison to our experimental measurements (continuous black lines).

## 5. Conclusions

In this work a Monte Carlo approach developed for modeling the electron transport in metallic samples was described. Our approach is capable to deliver the accurate calculation of the secondary electron emission spectra and of the electron yield

curves. We have simulated these characteristics for three different metals, that is copper, silver and gold. MC simulations were carried out also to investigate how tuning the metals' work functions may affect the secondary electron yields. We found out that a remarkable agreement between simulated and experimental yield spectra could be reached by setting the values of the work functions for the different metals very close to those obtained experimentally [30]. As a further improvement of our MC code suite, the possibility to model a tailored target surface morphology will be introduced, in order to investigate the effect that a given shape can have [48] in increasing or decreasing the electron yield according to the needed application.

## Acknowledgments

NMP is supported by the European Commission under the Graphene Flagship Core 2 grant No. 785219 (WP14, 'Composites') and FET Proactive ('Neurofibres') grant No. 732344 as well as by the Italian Ministry of Education, University and Research (MIUR) under the 'Departments of Excellence' grant L.232/2016. The authors gratefully acknowledge the Gauss Centre for Supercomputing for funding this project by providing computing time on the GCS Supercomputer JUQUEEN at Jülich Supercomputing Centre (JSC) [49]. Furthermore, the authors acknowledge FBK for providing unlimited access to the KORE computing facility.

## ORCID iDs

Roberto Cimino <https://orcid.org/0000-0002-7584-1950>  
 Nicola M Pugno <https://orcid.org/0000-0003-2136-2396>  
 Simone Taioli <https://orcid.org/0000-0003-4010-8000>

## References

- [1] Pierron J, Inguibert C, Belhaj M, Gineste T, Puech J and Raine M 2017 Electron emission yield for low energy electrons: Monte carlo simulation and experimental comparison for Al, Ag, and Si *J. Appl. Phys.* **121** 215107
- [2] Swanson C and Kaganovich I D 2016 Modeling of reduced effective secondary electron emission yield from a velvet surface *J. Appl. Phys.* **120** 213302
- [3] Seiler H 1983 Secondary electron emission in the scanning electron microscope *J. Appl. Phys.* **54** R1–8
- [4] Goldstein J I, Newbury D E, Michael J R, Ritchie N W M, Scott J H J and Joy D C 2017 *Scanning Electron Microscopy and X-Ray Microanalysis* (Berlin: Springer)
- [5] Sauli F 1997 Gem: a new concept for electron amplification in gas detectors *Nucl. Instrum. Methods Phys. Res. A* **386** 531–4
- [6] Benlloch J, Bressan A, Capeáns M, Gruwé M, Hoch M, Labbé J C, Placci A, Ropelewski L and Sauli F 1998 Further developments and beam tests of the gas electron multiplier (gem) *Nucl. Instrum. Methods Phys. Res. A* **419** 410–7
- [7] Lyneis C M, Schwettman H A and Turneaure J P 1977 Elimination on electron multipacting in superconducting structures for electron accelerators *Appl. Phys. Lett.* **31** 541–3
- [8] Somersalo E, Proch D, Ylä-Oijala P and Sarvas J 1998 Computational methods for analyzing electron multipacting in rf structures *Part. Accel.* **59** 107–41

- [9] Cimino R, Collins I R, Furman M A, Pivi M, Ruggiero F, Rumolo G and Zimmermann F 2004 Can low-energy electrons affect high-energy physics accelerators? *Phys. Rev. Lett.* **93** 014801
- [10] Cimino R, Comisso M, Grosso D R, Demma T, Baglin V, Flammini R and Larciprete R 2012 Nature of the decrease of the secondary-electron yield by electron bombardment and its energy dependence *Phys. Rev. Lett.* **109** 064801
- [11] Larciprete R, Grosso D R, Comisso M, Flammini R and Cimino R 2013 Secondary electron yield of Cu technical surfaces: dependence on electron irradiation *Phys. Rev. Spec. Top. Accel. Beams* **16** 011002
- [12] Cimino R and Demma T 2014 Electron cloud in accelerators *Int. J. Mod. Phys. A* **29** 1430023
- [13] Baglin V, Bojko J, Gröbner O, Taborelli M, Henrist B, Hilleret N, Scheuerlein C and Taborelli M 2000 The secondary electron yield of technical materials and its variation with surface treatments *Technical Report LHC-Project-Report-433*, CERN
- [14] Vallgren C Y et al 2011 Amorphous carbon coatings for the mitigation of electron cloud in the cern super proton synchrotron *Phys. Rev. Spec. Top. Accel. Beams* **14** 071001
- [15] Montero I, Aguilera L, Dávila M E, Nistor V C, González L A, Galán L, Raboso D and Ferritto R 2014 Secondary electron emission under electron bombardment from graphene nanoplatelets *Appl. Surf. Sci.* **291** 74–7
- [16] Valizadeh R, Malyshev O B, Wang S, Zolotovskaya S A, Allan Gillespie W and Abdolvand A 2014 Low secondary electron yield engineered surface for electron cloud mitigation *Appl. Phys. Lett.* **105** 231605
- [17] Valizadeh R, Malyshev O B, Wang S, Sian T, Cropper M D and Sykes N 2017 Reduction of secondary electron yield for e-cloud mitigation by laser ablation surface engineering *Appl. Surf. Sci.* **404** 370–9
- [18] Calatroni S et al 2017 First accelerator test of vacuum components with laser-engineered surfaces for electron-cloud mitigation *Phys. Rev. Accel. Beams* **20** 113201
- [19] Lai S T 2012 *Fundamentals of Spacecraft Charging: Spacecraft Interactions with Space Plasmas* (Princeton, NJ: Princeton University press)
- [20] Vaughan J R M 1989 A new formula for secondary emission yield *IEEE Trans. Electron Devices* **36** 1963–7
- [21] Dionne G F 1975 Origin of secondary-electron-emission yield-curve parameters *J. Appl. Phys.* **46** 3347–51
- [22] Shih A, Yater J, Hor C and Abrams R 1997 Secondary electron emission studies *Appl. Surf. Sci.* **111** 251–8
- [23] Lin Y and Joy D C 2005 A new examination of secondary electron yield data *Surf. Interface Anal.* **37** 895–900
- [24] Xie A-G, Zhao H-F, Song B and Pei Y-J 2009 The formula for the secondary electron yield at high incident electron energy from silver and copper *Nucl. Instrum. Methods Phys. Res. B* **267** 1761–3
- [25] Dapor M 2011 Secondary electron emission yield calculation performed using two different monte carlo strategies *Nucl. Instrum. Methods Phys. Res. B* **269** 1668–71
- [26] Mott N F 1929 The scattering of fast electrons by atomic nuclei *Proc. R. Soc. A* **124** 425
- [27] Ritchie R H 1957 Plasma losses by fast electrons in thin films *Phys. Rev.* **106** 874
- [28] Werner W S M, Glantschnig K and Ambrosch-Draxl C 2009 Optical constants and inelastic electron-scattering data for 17 elemental metals *J. Phys. Chem. Ref. Data* **38** 1013–92
- [29] Cimino R, Gonzalez L A, Larciprete R, Di Gaspare A, Iadarola G and Rumolo G 2015 Detailed investigation of the low energy secondary electron yield of technical cu and its relevance for the lhc *Phys. Rev. Spec. Top. Accel. Beams* **18** 051002
- [30] Gonzalez L A, Angelucci M, Larciprete R and Cimino R 2017 The secondary electron yield of noble metal surfaces *AIP Adv.* **7** 115203
- [31] Gergely G 2002 Elastic backscattering of electrons: determination of physical parameters of electron transport processes by elastic peak electron spectroscopy *Prog. Surf. Sci.* **71** 31–88
- [32] Sulyok A, Gergely G and Gruzza B 1992 Spectrometer corrections for a retarding field analyser used for elastic peak electron spectroscopy and auger electron spectroscopy *Acta Phys. Hung.* **72** 107
- [33] Dapor M 2017 *Transport of Energetic Electrons in Solids (Springer Tracts in Modern Physics)* (Cham: Springer)
- [34] Jablonski A, Salvat F and Powell C J 2004 Comparison of electron elastic-scattering cross sections calculated from two commonly used atomic potentials *J. Phys. Chem. Ref. Data* **33** 409–51
- [35] Salvat F, Martinez J D, Mayol R and Parellada J 1987 Analytical Dirac–Hartree–Fock–Slater screening function for atoms ( $Z = 1–92$ ) *Phys. Rev. A* **36** 467–74
- [36] Jablonski A, Salvat F, Powell C J and Lee A Y 2016 *NIST Electron Elastic-Scattering Cross-Section Database Version 4.0 (NIST Standard Reference Database vol 64)* (Gaithersburg, MD: National Institute of Standards and Technology)
- [37] Salvat F, Jablonski A and Powell C J 2005 Elsepa—Dirac partial-wave calculation of elastic scattering of electrons and positrons by atoms, positive ions and molecules *Comput. Phys. Commun.* **165** 157–90
- [38] Azzolini M, Morresi T, Garberoglio G, Calliari L, Pugno N M, Taioli S and Dapor M 2017 Monte carlo simulations of measured electron energy-loss spectra of diamond and graphite: role of dielectric-response models *Carbon* **118** 299–309
- [39] Taioli S, Umari P and De Souza M M 2009 Electronic properties of extended graphene nanomaterials from gw calculations *Phys. Status Solidi b* **246** 2572–6
- [40] Narayan R D, Miranda R and Rez P 2011 Simulating gamma-ray energy resolution in scintillators due to electron-hole pair statistics *Nucl. Instrum. Methods Phys. Res. B* **269** 2667–75
- [41] Narayan R D, Miranda R and Rez P 2012 Monte carlo simulation for the electron cascade due to gamma rays in semiconductor radiation detectors *J. Appl. Phys.* **111** 064910
- [42] Tanuma S, Powell C J and Penn D R 2011 Calculations of electron inelastic mean free paths. IX. Data for 41 elemental solids over the 50 eV to 30 keV range *Surf. Interface Anal.* **43** 689
- [43] Montanari C C, Miraglia J E, Heredia-Avalos S, Garcia-Molina R and Abril I 2007 Calculation of energy-loss straggling of C, Al, Si, and Cu for fast H, He, and Li ions *Phys. Rev. A* **75** 022903
- [44] Denton C D, Abril I, Garcia-Molina R, Moreno-Marín J C and Heredia-Avalos S 2008 Influence of the description of the target energy-loss function on the energy loss of swift projectiles *Surf. Interface Anal.* **40** 1481–7
- [45] Zeze D, Bideux L, Gruzza B, Gofek F, Daňko D and Mroz S 1997 Retarding field analyser used in elastic peak electron spectroscopy *Vacuum* **48** 399–401
- [46] Gruzza B, Chelda S, Robert-Goumet C, Bideux L and Monier G 2010 Monte carlo simulation for multi-mode elastic peak electron spectroscopy of crystalline materials: effects of surface structure and excitation *Surf. Sci.* **604** 217–26
- [47] Kawano H 2008 Effective work functions for ionic and electronic emissions from mono- and polycrystalline surfaces *Prog. Surf. Sci.* **83** 1–165
- [48] Ye M, Wang D and He Y 2017 Mechanism of total electron emission yield reduction using a micro-porous surface *J. Appl. Phys.* **121** 124901
- [49] Jülich Supercomputing Centre 2015 JUQUEEN: IBM Blue Gene/Q supercomputer system at the Jülich supercomputing centre *J. Large-Scale Res. Facil.* **1** 1–5